

ARTICLE OPEN



Coexisting charge density wave and ferromagnetic instabilities in monolayer InSe

Evgeny A. Stepanov ¹✉, Viktor Harkov ^{2,3}, Malte Rösner ⁴, Alexander I. Lichtenstein ^{2,3,5}, Mikhail I. Katsnelson ⁴ and Alexander N. Rudenko ⁴✉

Recently fabricated InSe monolayers exhibit remarkable characteristics that indicate the potential of this material to host a number of many-body phenomena. In this work, we systematically describe collective electronic effects in hole-doped InSe monolayers using advanced many-body techniques. To this end, we derive a realistic electronic-structure model from first principles that takes into account the most important characteristics of this material, including a flat band with prominent van Hove singularities in the electronic spectrum, strong electron-phonon coupling, and weakly screened long-ranged Coulomb interactions. We calculate the temperature-dependent phase diagram as a function of band filling and observe that this system is in a regime with coexisting charge density wave and ferromagnetic instabilities that are driven by strong electronic Coulomb correlations. This regime can be achieved at realistic doping levels and high enough temperatures, and can be verified experimentally. We find that the electron-phonon interaction does not play a crucial role in these effects, effectively suppressing the local Coulomb interaction without changing the qualitative physical picture.

npj Computational Materials (2022)8:118; <https://doi.org/10.1038/s41524-022-00798-4>

INTRODUCTION

Two-dimensional (2D) group III–VI metal chalcogenides have recently attracted great interest because of their appealing characteristics. Among them are high charge carrier mobility, controllable energy gaps, excellent thermoelectric and optical properties, as well as excellent stability at ambient conditions^{1–6}. The electronic structure of ultrathin InSe features flat regions in the valence band dispersion leading to prominent van Hove singularities (vHS) in the hole density of states (DOS)⁷. Importantly, this kind of electronic structure is only observed in the monolayer limit of these materials, as has been experimentally demonstrated by means of angular resolved photoemission spectroscopy^{8,9}. If the vHS appears at the Fermi energy, it may result in numerous competing channels of instabilities such as magnetic, charge, or superconducting order with a very non-trivial interplay between them^{10–12}. Scientific interest to flat-band materials has been triggered in recent years by the discovery of unconventional superconductivity and related exotic phenomena in twisted bilayer graphene^{13–15}. Therefore, thin films group III–VI materials turn out to be prospective candidates for studying many-body correlation effects, which are closely related to the above-mentioned features in the electronic spectrum¹⁶, circumventing the need for any twist engineering.

The theoretical description of many-body effects in monolayer InSe is challenging and is limited to a few works mainly focusing on the electron-phonon coupling. In particular, it has been shown that hole states in this material undergo significant renormalization due to the interaction with acoustic phonons, which gives rise to the appearance of unusual temperature-dependent optical excitations¹⁷. Also, a strong electron-phonon interaction may result in a charge density wave (CDW) instability predicted

recently¹⁸. At the same time, monolayer InSe is expected to possess strong many-body electronic effects that have not been accurately studied yet. For instance, the presence of the Mexican-hat-like band in this material might favor a magnetic instability that could lead to the formation of a magnetically ordered state at low temperatures. Up to now the existence of a magnetic solution for InSe monolayer has been demonstrated based on density functional theory (DFT)¹⁹ without systematic consideration of many-body effects. In addition, the weakly screened Coulomb interaction in 2D may result in a Coulomb-driven CDW instability. However, a systematic many-body consideration of these effects is still missing in the literature.

In this work, we address the problem of collective electronic effects in monolayer InSe. For this purpose, we derive a realistic model that considers both, long-range Coulomb interactions and the electron-phonon coupling. The introduced interacting electronic problem is further solved using an advanced many-body approach that explicitly takes into account non-local collective electronic fluctuations. In the regime of hole-doping, we find that charge ordering represents the main instability. It is formed in a broad range of doping levels and corresponds to a commensurate CDW, which indicates that this instability is rather driven by strong electronic Coulomb correlations than by an electron-phonon mechanism as discussed previously. Inside the CDW phase, we detect another collective effect that drives the system towards a ferromagnetic (FM) ordering. This instability is formed in close proximity to the vHS in the DOS. Finally, we observe that the electron-phonon coupling tends to suppress the FM ordering, enlarging the CDW phase. However, the presence of the electron-phonon coupling does not qualitatively affect the observed effects.

¹CPHT, CNRS, Ecole Polytechnique, Institut Polytechnique de Paris, F-91128 Palaiseau, France. ²I. Institute of Theoretical Physics, University of Hamburg, Notkestraße 9, 22607 Hamburg, Germany. ³European X-Ray Free-Electron Laser Facility, Holzkoppel 4, 22869 Schenefeld, Germany. ⁴Radboud University, Institute for Molecules and Materials, 6525AJ Nijmegen, The Netherlands. ⁵The Hamburg Centre for Ultrafast Imaging, Luruper Chaussee 149, 22761 Hamburg, Germany. [✉]email: evgeny.stepanov@polytechnique.edu; a.rudenko@science.ru.nl

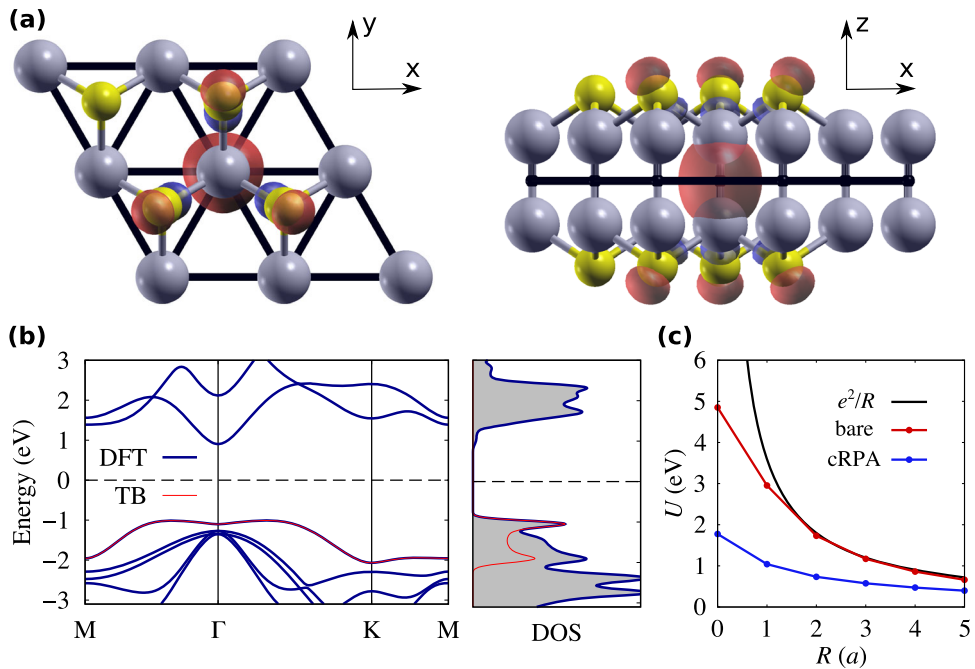


Fig. 1 First-principle calculation of model parameters. **a** Schematic crystal structure of monolayer InSe shown in two projections. Superimposed is an isosurface of the Wannier function describing the valence states in InSe. The black lines depict an effective electronic lattice; **(b)** Band structure and DOS calculated in DFT (blue), and from tight-binding model parametrization (red); **(c)** The Coulomb interaction between the Wannier orbitals shown as a function of the distance calculated within the cRPA scheme. The bare (unscreened) Coulomb interaction is shown for comparison.

RESULTS

Model

InSe is a layered van der Waals material, where each layer consists of two vertically displaced In-Se honeycombs, giving rise to four Se-In-In-Se atomic planes (Fig. 1a). Each layer has D_{3h} point group symmetry. In the monolayer limit DFT calculations predict InSe to be a semiconductor with an indirect energy gap of ~ 2 eV. The electronic dispersion shows a single well-separated valence band, which has the shape of a Mexican hat, as depicted in Fig. 1b. This shape is characterized by a ring of radius $k_0 \approx 0.3 \text{ \AA}^{-1}$ formed by the valence band edge, and by a well of $E_0 = 0.09$ eV deep at the Γ point. These parameters are in reasonable agreement with those obtained from photoemission spectroscopy in Ref. ⁸. This peculiar band structure is of great advantage for many-body considerations as it allows us to reduce the correlated subspace to a single band. To this end, we construct a tractable tight-binding model that accurately reproduces this highest valence band (Fig. 1b). The corresponding model is defined in terms of maximally localized Wannier functions on an effective triangular lattice, as shown in Fig. 1a. Each Wannier function is reminiscent of an In-In bonding orbital with tails on Se atoms. The resulting single-band model Hamiltonian on a triangular lattice reads

$$H = \sum_{ij,\sigma} t_{ij} c_{i\sigma}^\dagger c_{j\sigma} + U \sum_i n_{i\uparrow} n_{i\downarrow} + \frac{1}{2} \sum_{i \neq j, \sigma \sigma'} V_{ij} n_{i\sigma} n_{j\sigma'} + \omega_{\text{ph}} \sum_i b_i^\dagger b_i + g \sum_{i,\sigma} n_{i\sigma} (b_i + b_i^\dagger) \quad (1)$$

where $c_{i\sigma}^\dagger$ operator annihilates (creates) an electron on the site i with the spin projection $\sigma = \uparrow, \downarrow$. The ab initio electronic dispersion is reproduced by five neighboring hopping amplitudes t_{ij} : $t_{01} = 127.9$ meV, $t_{02} = -41.8$ meV, $t_{03} = -45.0$ meV, $t_{04} = 13.0$ meV, and $t_{05} = -4.4$ meV. We neglect spin-orbit coupling because it is not important in truly 2D crystals with the mirror symmetry²⁰, which is also supported by earlier DFT calculations showing that the relevant valence states in monolayer InSe remain unaffected by the presence of spin-orbit coupling²¹.

Figure 1c shows the bare and screened Coulomb interaction between the Wannier orbitals calculated as a function of R within the constrained random phase approximation (cRPA) to avoid a double counting of the screening channels from the correlated subspace (see Methods for more details). $R(a)$ corresponds to the distance between the sites of an effective triangular lattice and is expressed in units of the lattice constant a . The on-site screened Coulomb repulsion $U = 1.78$ eV greatly exceeds the bandwidth ~ 1 eV, which usually indicates strong magnetic fluctuations in the system²². As expected for a 2D material²³, the non-local Coulomb interaction V_{ij} in monolayer InSe is weakly screened and long-ranged (see blue line in Fig. 1c). Weak long-range screening in 2D is a direct consequence of the reduced dimensionality. In particular, the softer \mathbf{q} -dependence of the bare Coulomb interaction $V^B(q) = 2\pi e^2/q$ (in contrast to $\sim 1/q^2$ in 3D) ensures that the dielectric constant $\epsilon(\mathbf{q}, \omega) \rightarrow 1$ as $\mathbf{q} \rightarrow 0$ for any gapped 2D system (see, e.g., Ref. ²⁴). At finite wave vectors this behavior is less obvious, yet the trend is similar^{23,25,26}. Thus, cRPA Coulomb matrix elements for layered materials indeed show as a general trend the described weakly screened and long-ranged behavior with graphene²⁷ and NbS_2 ²⁸ being representative metallic examples. Moreover, in monolayer InSe the interaction $V_{01} = 1.04$ eV between nearest-neighbor electronic densities $n_{i\sigma} = c_{i\sigma}^\dagger c_{i\sigma}$ is larger than the half of the on-site Coulomb repulsion U . This suggests that the considered system may have a tendency to form a CDW phase due to the competition between local and non-local Coulomb interactions^{29,30}. The full form of the long-range Coulomb interaction is presented in Methods.

To estimate the phonon properties without double counting screening channels from the correlated subspace we utilize the constrained Density Functional Perturbation Theory (cDFPT)³¹ at hole doping. We find that the effective electron-phonon coupling $\lambda = 2 \int d\omega \frac{d^2 F(\omega)}{\omega}$ is dominated by a rather sharp resonance at low phonon frequency, which we can approximate with a local phonon model, i.e. $a^2 F(\omega) = N_0 g^2 \delta(\omega - \omega_{\text{ph}})$. Here, N_0 is the DOS at

the Fermi level, $\omega_{\text{ph}} = 8.5$ meV the phonon energy, and $g = 34.7$ meV its coupling strength to the topmost valence band (see Methods). The strong local coupling of electrons to phonons renders the CDW formation even more favorable. Indeed, upon integrating out bosonic operators $b^{(\dagger)}$ that correspond to phonon degrees of freedom one gets an effective local frequency-dependent attractive interaction $U_{\omega}^{\text{ph}} = 2g^2 \frac{\omega_{\text{ph}}}{\omega^2 - \omega^2}$ that reduces the repulsive on-site Coulomb potential as $U^{\text{ph}} \rightarrow U - U^{\text{ph}}$ ^{32–34} and thus enhances the effect of the non-local Coulomb interaction V_{ij} .

An accurate theoretical investigation of many-body instabilities in InSe monolayer cannot be performed within conventional perturbative methods like the random phase approximation^{35–37} or the GW approach^{38–40}. Local correlation effects that are governed by such a large value of the local Coulomb interaction U require a systematic many-body consideration using, e.g., the dynamical mean-field theory (DMFT)⁴¹. At the same time, spatial collective electronic fluctuations and the long-range Coulomb interaction cannot be captured by DMFT and require diagrammatic extensions of this theory⁴². In this work, we solve the considered many-body problem using the dual triply irreducible

local expansion (D-TRILEX) method^{43–45} that allows one to account for leading collective electronic fluctuations on equal footing without any limitation on the range⁴⁶. More details on the theoretical approach are provided in Methods.

Collective electronic instabilities

One of the most remarkable features of the InSe monolayer is the presence of a Mexican-hat-like valence band in the electronic dispersion^{8,9}. The top of this band exhibits flat regions that lead to a sharp vHS in the DOS. However, under normal conditions this valence band is fully filled, making the material an indirect semiconductor. To enhance correlation effects in the system we consider realistic hole dopings with the Fermi level close to the vHS^{10–12}. Practically, high concentration of holes of the order of 10^{14} cm^{-2} can be achieved in 2D materials by means of electrostatic solid- or liquid-electrolyte gating⁴⁷ or by surface molecular doping⁴⁸. First, we solve the many-body problem without considering the electron–phonon coupling in order to investigate purely Coulomb correlation effects. For detecting main instabilities in the system we perform single-shot D-TRILEX calculations for the charge and spin susceptibilities $X_{\mathbf{q},\omega}^c$. In this case, divergences of charge and spin susceptibilities do not affect each other through the self-energy, which allows one to detect instabilities inside broken-symmetry phases (see Methods for more details). Fig. 2 shows the obtained phase diagram for the InSe monolayer, where $\langle n \rangle$ is the filling of the considered valence band ($\langle n \rangle = 2$ in the fully filled band that corresponds to the undoped case). Phase boundaries indicate points in the temperature (T) vs. doping space, where corresponding susceptibilities diverge. We find that the charge susceptibility diverges in a broad range of hole dopings $\langle n \rangle \geq 1.29$, and the corresponding phase boundary is independent of temperature. Fig. 3a displays the momentum resolved charge susceptibility $X_{\mathbf{q},\omega}^c$ obtained at the zero frequency $\omega = 0$ near the transition point ($T = 300$ K, $\langle n \rangle = 1.29$). It shows that the corresponding Bragg peaks in the charge susceptibility appear at the K points of the Brillouin zone (BZ), which indicates the formation of a commensurate CDW ordering. In turn, the spin susceptibility remains finite at the CDW transition point and diverges only inside the CDW phase. The corresponding instability has a dome shape as depicted in Fig. 2 by a blue dashed line. Remarkably, we find that the top of the dome corresponds to the filling $\langle n \rangle = 1.70$ at which the vHS appears exactly at the Fermi level. The momentum resolved spin susceptibility obtained close to the top of the dome ($T = 375$ K, $\langle n \rangle = 1.70$) is shown in Fig. 3b. It reveals a sharp Bragg peak at the Γ point of the BZ, which indicates the tendency towards FM ordering.

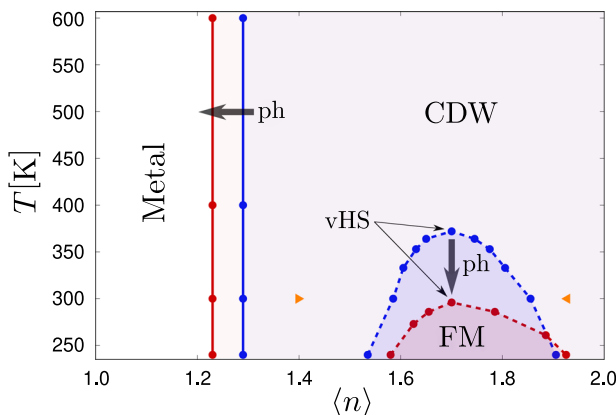


Fig. 2 Phase diagram for the monolayer InSe as a function of temperature and doping. Solid vertical lines correspond to the CDW phase boundaries, dashed lines depict the FM instabilities. Results are obtained in the presence (red line) and in the absence (blue line) of the electron–phonon coupling. The top of the FM dome corresponds to the filling $\langle n \rangle = 1.70$ at which the vHS appears at the Fermi energy. Black arrows with the label “ph” illustrate the effect of phonons that tend to suppress the FM instability and favor the CDW ordering. Orange triangles indicate the CDW transition points $\langle n \rangle = 1.40$ and $\langle n \rangle = 1.92$ obtained at $T = 300$ K taking into account the electron–phonon coupling in the absence of the non-local Coulomb interaction.

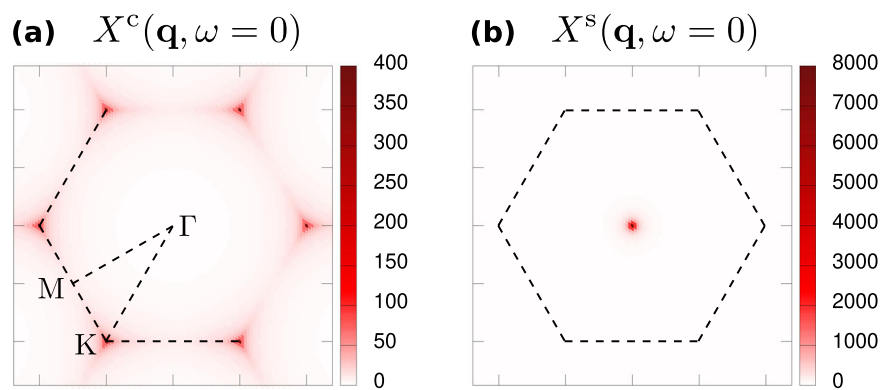


Fig. 3 Momentum resolved susceptibilities $X_{\mathbf{q},\omega}^c$, $X_{\mathbf{q},\omega}^s$ calculated at zero frequency $\omega = 0$ in the absence of the electron–phonon coupling. Results are obtained close to the CDW ($T = 300$ K, $\langle n \rangle = 1.29$) and the FM ($T = 375$ K, $\langle n \rangle = 1.70$) instabilities, respectively. Bragg peaks that appear in the charge susceptibility (a) at the K points of the hexagonal BZ correspond to a commensurate CDW ordering. A single peak at the Γ point in the spin susceptibility (b) confirms that the observed instability is FM.

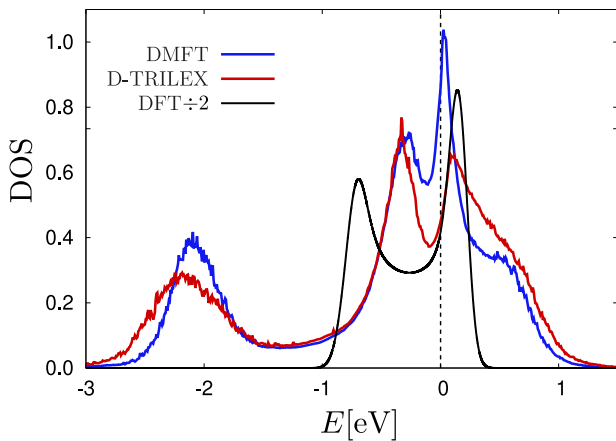


Fig. 4 DOS of the InSe monolayer. Results are obtained within DMFT (blue), D-TRILEX (red), and DFT (black) methods close to a CDW phase boundary at $T = 300$ K and $\langle n \rangle = 1.29$ without taking into account the electron–phonon coupling. Note that the DOS of DFT is divided by a factor of 2 for easier comparison.

Electronic density of states

The obtained phase diagram illustrates that the commensurate CDW represents the main instability in the InSe monolayer contrary to the DFT prediction¹⁹. The formation of this phase is associated with strong long-range collective charge fluctuations that are expected to renormalize the electronic dispersion. Therefore, the development of the CDW ordering should also be reflected in single-particle observables such as the electronic DOS. In order to account for the feedback effects of long-range collective electronic fluctuations to single-particle quantities^{49,50} we perform self-consistent D-TRILEX calculations^{43–45}. The obtained result is compared to the one of the DMFT that does not take into account spatial correlation effects. Fig. 4 shows the DOS calculated close to the CDW phase boundary ($T = 300$ K and $\langle n \rangle = 1.29$). We find that the DOS obtained within DMFT (blue) is similar to the one of DFT (black) and shows a sharp peak in the vicinity of the Fermi energy, which reflects the presence of the vHS in the electronic spectrum. However, if one includes the effect of spatial correlations via the D-TRILEX approach, one observes that at the transition point this peak turns into a pseudogap (red). In this particular case, the pseudogap appears due to strong collective charge fluctuations that lead to an almost diverged charge susceptibility $X_{\mathbf{q}\omega}^c$ at the $\mathbf{q} = \mathbf{K}$ point of the BZ close to a phase transition. As a consequence, the renormalized interaction $W_{\mathbf{q}\omega}^c$ that enters the self-energy also becomes nearly divergent, which causes the formation of a pseudogap according to the tendency towards electron–hole pairing. This mechanism is similar to the formation of the excitonic insulator state^{51–53} with the only difference that in our case electrons and holes belong to the same band and that excitons in the condensate have non-zero momentum corresponding to the CDW wave vector. If the tendency towards electron–hole pairing results in long-range order, one gets a true gap whereas strong short-range order without long-range order leads to a pseudogap in the electronic spectrum^{54,55}.

Effect of the electron–phonon coupling

In order to investigate the effect of phonons on the observed instabilities we repeat the same calculation in the presence of the electron–phonon coupling. As Fig. 2 shows, in this case the CDW phase boundary is shifted to smaller values of the filling $\langle n \rangle = 1.23$. At the same time, the FM instability is pushed down to lower temperatures, but the top of the FM dome remains at the vHS filling $\langle n \rangle = 1.70$ as in the absence of phonons. This result is

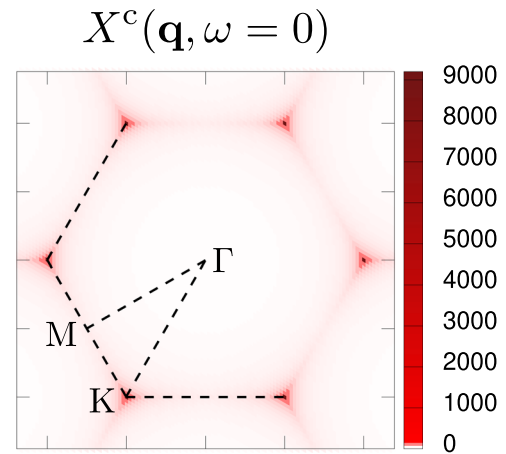


Fig. 5 Momentum resolved charge susceptibility $X^c(\mathbf{q}, \omega = 0)$. Result is obtained close to the CDW transition point $T = 300$ K and $\langle n \rangle = 1.23$ taking into account the electron–phonon coupling.

consistent with the fact that the electron–phonon coupling effectively reduces the on-site Coulomb potential, which consequently decreases the critical temperature for the magnetic instability. The observed shift of the CDW phase boundary can also be explained by the same argument. Indeed, the local Coulomb repulsion favors single occupation of lattice sites. On the contrary, the non-local Coulomb interaction promotes the CDW ordering, which upon reducing the local Coulomb interaction becomes energetically preferable.

Remarkably, Fig. 5 demonstrates that taking into account the electron–phonon coupling does not change the position of Bragg peaks in the charge susceptibility calculated close to the CDW phase transition point $T = 300$ K and $\langle n \rangle = 1.23$. As in the absence of phonons, the momentum-space structure of this susceptibility $X_{\mathbf{q}}^c(\omega = 0)$ consists of six delta-function-like Bragg peaks that appear at K points of the BZ. This fact illustrates that the developed charge ordering also corresponds to a commensurate CDW. Moreover, we do not observe any additional Bragg peaks in the charge susceptibility at twice the Fermi wave vector $\mathbf{q}^* = 2\mathbf{k}_F$, which would indicate a tendency to the charge ordering due to the electron–phonon mechanism.

The effect of phonons can be revealed only upon excluding the contribution of the non-local Coulomb interaction $V_{\mathbf{q}}$ from the charge susceptibility. In this case, an additional exclusion of phonons eliminates both sources of the CDW instability, and $X_{\mathbf{q}\omega}^c$ remains finite at any filling. If the electron–phonon coupling is taken into account, the maximum value of $X_{\mathbf{q}}^c(\omega = 0)$ corresponds to the wave vector \mathbf{q}^* that changes with doping. For instance, at $\langle n \rangle = 1.23$ this wave vector lies between Γ and \mathbf{K} points of the BZ (Fig. 6a). However, the value of this susceptibility is negligibly small compared to the almost diverged one calculated in the presence of the non-local Coulomb interaction (see Fig. 5). Increasing the filling, the maximum of the charge susceptibility calculated for the case of $V_{\mathbf{q}} = 0$ also increases, and the corresponding wave vector \mathbf{q}^* shifts towards the \mathbf{K} point of the BZ (Fig. 6b). At $\langle n \rangle \simeq 1.40$ ($T = 300$ K) the \mathbf{q}^* reaches the \mathbf{K} point (Fig. 6c), and the charge susceptibility diverges. This means that the CDW instability mediated purely by phonons is shifted to much larger values of the filling compared to the one driven by strong Coulomb correlations (orange triangles in Fig. 2). Increasing the filling even more, the charge susceptibility becomes finite again at $\langle n \rangle = 1.92$ (Fig. 6d). Remarkably, Figs. 6c and d show that Bragg peaks that correspond to CDW ordering vectors \mathbf{q}^* are drastically different for two fillings $\langle n \rangle = 1.40$ and $\langle n \rangle = 1.92$. This means that the ordering vector of the phonon-driven CDW also changes inside the CDW phase. These results confirm that the

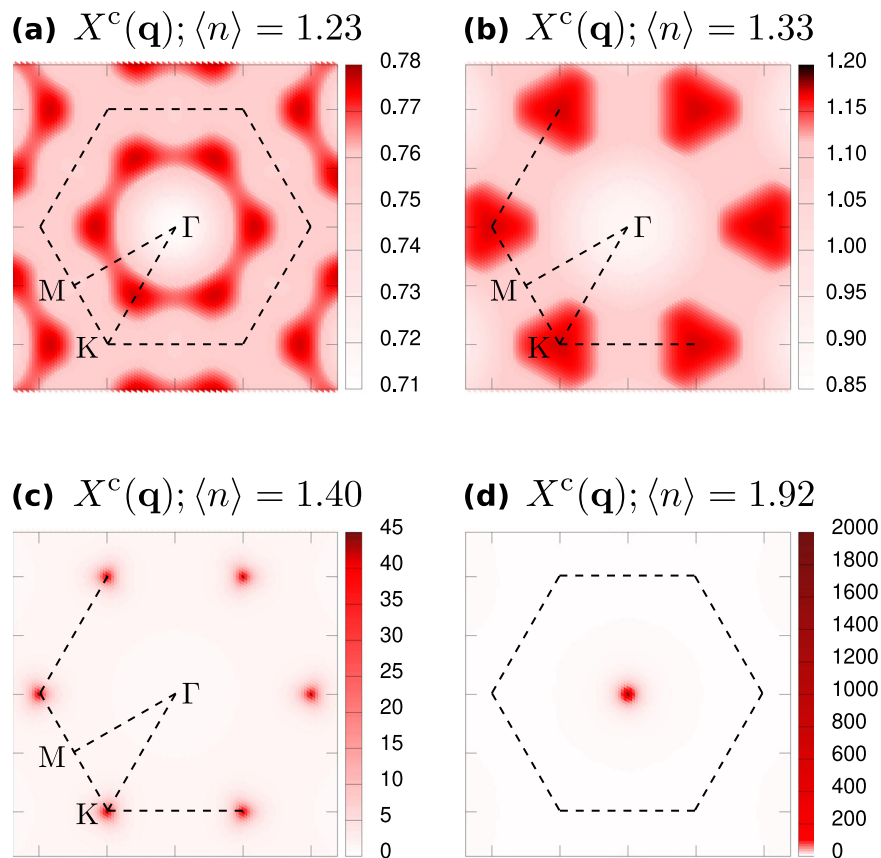


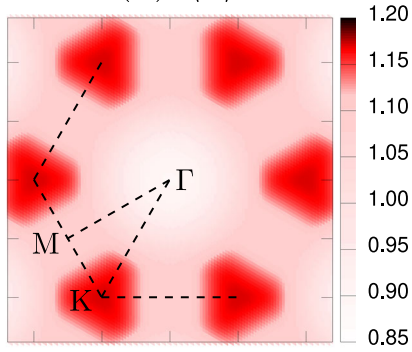
Fig. 6 Momentum resolved charge susceptibility $X^c(\mathbf{q})$ calculated at zero frequency $\omega = 0$. Results are obtained at $T = 300$ K for different values of the filling $\langle n \rangle = 1.23$ (a), $\langle n \rangle = 1.33$ (b), $\langle n \rangle = 1.40$ (c), and $\langle n \rangle = 1.92$ (d) taking into account the electron–phonon coupling and excluding the effect of the non-local Coulomb interaction ($V_{\mathbf{q}} = 0$).

metal-to-CDW phase transition in the monolayer InSe is driven by strong Coulomb correlations rather than by the electron–phonon mechanism as suggested previously¹⁸.

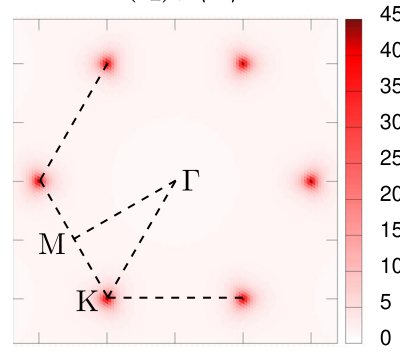
The momentum-structure of the spin susceptibility also changes with doping. At the CDW transition point it stays finite and has a Néel antiferromagnetic (AFM) behavior that manifests itself in the largest value of the susceptibility at K point of the BZ (Fig. 7a). At a larger filling $\langle n \rangle = 1.42$ the Néel AFM form of the spin susceptibility changes to a more complex structure with the largest value at Γ point of the BZ, which indicates the FM instability, and less pronounced intensities at M points corresponding to row-wise AFM fluctuations (Fig. 7b). Increasing the filling to $\langle n \rangle = 1.70$ the van Hove singularity (vHS) in the electronic spectral function appears at the Fermi energy, which strongly enhances collective electronic fluctuations. Fig. 7c shows that close to the magnetic instability the spin susceptibility becomes purely FM, which is indicated by the single delta-function-like Bragg peak that at the Γ point of the BZ. At even larger filling of the band $\langle n \rangle = 1.92$ the spin susceptibility remains FM, but the value of the susceptibility at Γ point decreases compared to the case of the vHS filling (Fig. 7d), which confirms the dome-like structure of the FM instability.

For completeness, we also show the electronic DOS calculated close to the CDW phase transition point $T = 300$ K and $\langle n \rangle = 1.23$ in the presence of the electron–phonon coupling (Fig. 8). We find that in this case the effect of spatial correlations on the DOS is qualitatively the same as in the absence of phonons. Note that in this case DMFT considers the effect of the local electron–phonon coupling via the renormalized on-site Coulomb potential $U^* = U - U_{\omega}^{\text{ph}}$.

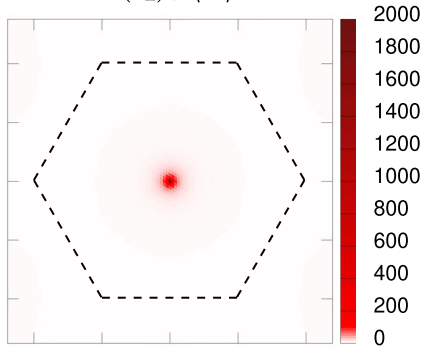
(b) $X^c(\mathbf{q}); \langle n \rangle = 1.33$



(c) $X^c(\mathbf{q}); \langle n \rangle = 1.40$



(d) $X^c(\mathbf{q}); \langle n \rangle = 1.92$



DISCUSSION

We have systematically studied many-body effects in the hole-doped InSe monolayer. We have found that this material displays coexisting instabilities that are mainly driven by non-local Coulomb correlations. The commensurate CDW ordering represents the main instability in the system and is revealed in a broad range of doping levels and temperatures. The presence of this ordering is confirmed by the appearance of a pseudogap in the DOS close to the transition point, which illustrates the importance of considering spatial electronic fluctuations. We also observed the tendency to a FM ordering that manifests itself only inside the CDW phase and is related to a vHS in the electronic spectrum. The inclusion of the electron–phonon coupling results in a shift of the CDW and FM ordering phases on the phase diagram, which can be explained by an effective reduction of the local Coulomb interaction. However, the qualitative physical picture does not change in the presence of phonons. Our results suggest that monolayer InSe can serve as an attractive playground for investigation of coexisting many-body correlation effects and, in particular, of 2D magnetism, although in a bulk phase this material is non-magnetic.

In general, the Coulomb-driven CDW instability in electronic systems appears as the result of a competition between local and non-local electron-electron interactions that favor different distribution of electrons on a lattice. In order to change the balance between these interactions, the free standing InSe monolayer considered here could be exposed to external dielectric screening as, e.g., resulting from a substrate or from encapsulation. This mechanism is especially effective in 2D as the environmental screening is non-local in layered materials, which reduces long-ranged interactions stronger than the on-site interaction^{25,26,56}. This kind of Coulomb engineering paves the

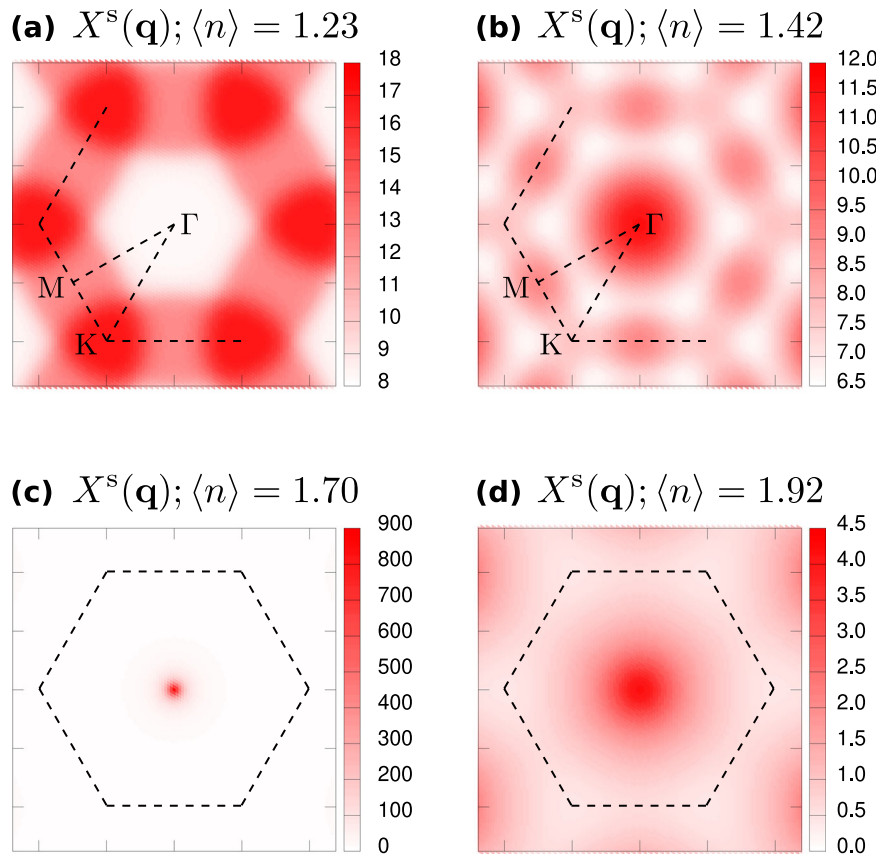


Fig. 7 Momentum resolved spin susceptibility $X^s(\mathbf{q})$ calculated at zero frequency $\omega = 0$ taking into account the electron–phonon coupling. Results are obtained at $T = 300$ K for different values of the filling $\langle n \rangle = 1.23$ (a), $\langle n \rangle = 1.42$ (b), $\langle n \rangle = 1.70$ (c), and $\langle n \rangle = 1.92$ (d).

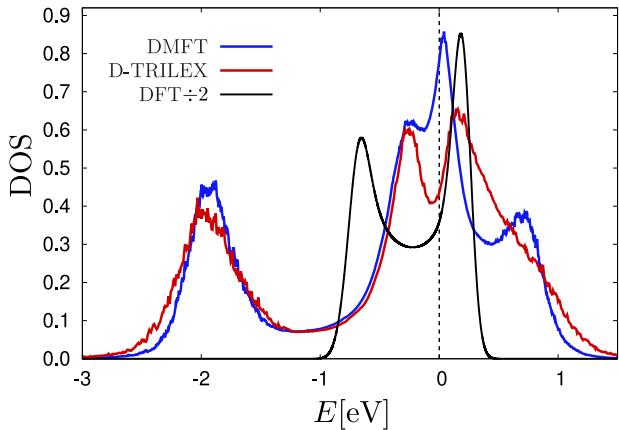


Fig. 8 DOS of the monolayer InSe. Results are obtained within DMFT (blue), D-TRILEX (red), and DFT (black) methods close to a CDW phase boundary at $T = 300$ K and $\langle n \rangle = 1.23$ taking into account the electron–phonon coupling. Note that the DOS of DFT is divided by a factor of 2 for easier comparison.

way for exploring additional degrees of freedom to tune the correlation effects in this 2D material.

METHODS

First-principle calculations

The band structure presented in Fig. 1b was calculated within density functional theory utilizing the projected augmented wave (PAW)

formalism^{57,58} as implemented in the Vienna *ab initio* simulation package (vasp)^{59,60} version 5.4. The exchange–correlation effects were considered using the generalized gradient approximation (GGA)⁶¹ and the standard In and Se pseudopotentials in version 5.4. A 500 eV energy cutoff for the plane-waves and a convergence threshold of 10^{-7} eV were used in the calculations together with tetrahedron method for all involved integrals. The Brillouin zone was sampled by a (36×36) \mathbf{k} -point mesh. We adopted fully relaxed atomic structure with a lattice constant of 3.94 \AA , In–In vertical distance of 2.76 \AA , and Se–Se vertical distance of 5.37 \AA . A $\sim 30 \text{ \AA}$ -thick vacuum layer was added in the direction perpendicular to the 2D plane in order to avoid spurious interactions between supercell images. The Wannier functions and the tight-binding Hamiltonian were calculated within the scheme of maximal localization^{62,63} using the WANNIER90 package⁶⁴ version 1.2.

The Coulomb interaction was evaluated using the maximally localized Wannier functions within the constrained random phase approximation (cRPA)^{65,66} as $U_{ij} = \langle w_i w_j | U | w_i w_j \rangle$, where U is the partially screened Coulomb interaction defined by $U = v + \nabla \Pi U$ with v being the bare Coulomb interaction, Π the cRPA polarization, and w_i is the Wannier function at the lattice site i . The polarization operator Π describes screening from all electronic states except those given by the tight-binding Hamiltonian obtained in the Wannier basis. For these calculations, we used a recent cRPA implementation by Kaltak within vasp⁶⁶. To converge the cRPA polarization with respect to the number of empty states with used in total 64 bands. To derive a light-weighted Coulomb model for arbitrary q -grids, we fitted the cRPA Coulomb interaction in momentum space according to:

$$U(q) = v(q)/\epsilon(q) \quad (2)$$

with the bare Coulomb interaction of a monolayer

$$v(q) = \frac{\hbar}{2\pi} \int_{-\pi/h}^{+\pi/h} \frac{4\pi e^2}{Vq^2} dq_z = \frac{4e^2 \arctan\left(\frac{\pi}{qh}\right)}{A} \quad (3)$$

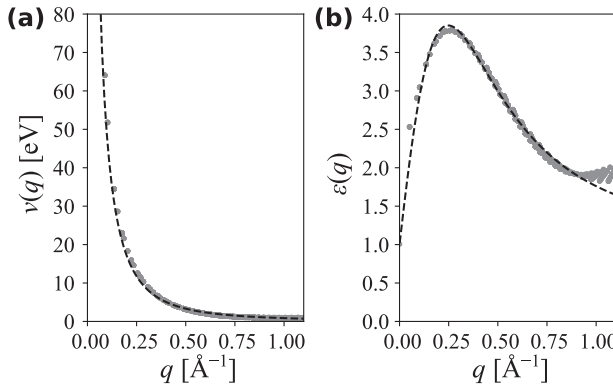


Fig. 9 Coulomb interaction from first-principle calculations. Bare Coulomb interaction (a) and cRPA dielectric function (b) within the Wannier basis. Markers represent ab initio data and dashed lines the corresponding fits.

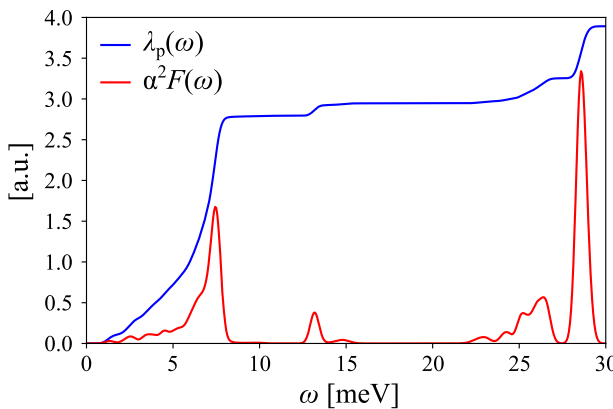


Fig. 10 Phonon properties from first-principle calculations. cDFPT Eliashberg function together with the partial effective electron-phonon coupling $\lambda_p(\omega) = 2 \int_0^\omega d\omega' \frac{\alpha^2 F(\omega')}{\omega'}$.

and the dielectric function

$$\epsilon(q) = \frac{\epsilon_0(q) + 1 - (\epsilon_0(q) - 1)e^{-qd}}{\epsilon_0(q) + 1 + (\epsilon_0(q) - 1)e^{-qd}} \quad (4)$$

with

$$\epsilon_0(q) = \frac{a + q^2}{\frac{a \sin(qc)}{bqc} + q^2}. \quad (5)$$

Here, e , A , and h are the elementary electron charge, the InSe unit cell area and its effective height, respectively, and a , b , c , and d are fitting parameter. In Fig. 9 we show the corresponding ab initio values together with their fits using $h = 15.35 \text{\AA}$, $a = 1.07 \text{\AA}^{-2}$, $b = 5.79$, $c = 0.14 \text{\AA}$, and $d = 8.09 \text{\AA}$. In this expression $\epsilon_0(q)$ represents the (semi-conducting) cRPA screening in the middle of the film, i.e., $z = 0$, which is assumed to be the same for the entire film thickness d and which we parameterized following Ref. ⁶⁷. The surrounding of the film is supposed to be vacuum. This defines a classical electrostatics problem, which can be analytically solved (see e.g., Ref. ⁶⁸). The full non-local cRPA background screening takes than the form of Eq. (4). More details on this can be found in Ref. ²⁶. The real-space U_{ij} are calculated via a conventional Fourier transform of $U(q)$ from Eq. (2) and using these fits.

The phonon properties are calculated within QUANTUM ESPRESSO⁶⁹ version 6.5 using norm-conserving pseudopotentials generated using the “atomic” code by A. Dal Corso (v.5.0.99 svn rev. 10869, 2014), the local density approximation, an energy cutoff of 80 Ry, and a finite hole doping of 0.04 holes per unit cell. For the initial constrained Density Functional Perturbation Theory (cDFPT)³¹ calculation we use (16×16) \mathbf{k} and (8×8) \mathbf{q} -point meshes and exclude the highest (hole doped) valence band within the evaluation of the Sternheimer equation. Afterwards we use the EPW code⁷⁰ version 5.0.0 to extrapolate the cDFPT results to (32×32) \mathbf{k} - and

\mathbf{q} -point meshes using a Wannier interpolation based on a single Wannier projection for the highest valence band (in the very same way as we constructed them in VASP for the cRPA calculations). This allows us to accurately calculate the cDFPT Eliashberg function $\alpha^2 F(\omega)$ as shown in Fig. 10. From this we calculate the effective electron-phonon coupling $\lambda = 2 \int d\omega \frac{\alpha^2 F(\omega)}{\omega}$ which we finally use to fit our local phonon model via $\alpha^2 F(\omega) \approx N_0 g^2 \delta(\omega - \omega_{\text{ph}})$ with $N_0 = 3.88 \text{ eV}^{-1}$ per spin per unit cell.

Many-body calculations

The introduced many-body electronic model (1) is solved using the finite-temperature diagrammatic D-TRILEX approach^{43–45}. In this method, local correlation effects are treated via the self-energy Σ_v^{imp} and the polarization operator Π_ω^{imp} of an effective local impurity problem of DMFT. These quantities are written in the fermionic (v) and bosonic (ω) Matsubara frequency space, respectively. The corresponding impurity problem is solved numerically exactly using the open source CT-HYB solver^{71,72} based on ALPS libraries⁷³.

Within the self-consistent calculations, the spatial fluctuations are considered in a partially bosonized form of the renormalized charge ($\zeta = c$) and spin ($\zeta = s$) interactions $W_{\mathbf{q}\omega}^\zeta$ that enter the diagrammatic part of the self-energy $\bar{\Sigma}_{\mathbf{kv}}$ introduced beyond DMFT^{43–45}. The dressed Green's function $G_{\mathbf{kv}}$ of the problem can be found using the standard Dyson equation $G_{\mathbf{kv}}^{-1} = iv + \mu - \epsilon_{\mathbf{k}} - \Sigma_{\mathbf{kv}}$ written in momentum \mathbf{k} space. In this expression μ is the chemical potential, $\epsilon_{\mathbf{k}}$ is the electronic dispersion that can be obtained as a Fourier transform of the hopping amplitudes t_{ij} and $\Sigma_{\mathbf{kv}} = \Sigma_v^{\text{imp}} + \bar{\Sigma}_{\mathbf{kv}}$ is the total self-energy. The renormalized interaction $W_{\mathbf{q}\omega}^\zeta$ can be found via the following Dyson equation $W_{\mathbf{q}\omega}^{\zeta-1} = U_{\mathbf{q}\omega}^{\zeta-1} - \Pi_{\mathbf{q}\omega}^{\zeta}$, where $U_{\mathbf{q}\omega}^c = U/2 - U_{\omega}^{\text{ph}} + V_{\mathbf{q}}$ and $U_{\mathbf{q}\omega}^s = -U/2$ are the bare interactions in the charge and spin channels, respectively^{43–45}. $\Pi_{\mathbf{q}\omega}^{\zeta} = \Pi_\omega^{\zeta \text{ imp}} + \bar{\Pi}_{\mathbf{q}\omega}^{\zeta}$ is the total polarization operator of the problem, where $\bar{\Pi}_{\mathbf{q}\omega}^{\zeta}$ is the diagrammatic contribution introduced in the D-TRILEX approach^{43–45}. In this way, the dressed lattice Green's function $G_{\mathbf{kv}}$ takes into account both, local and non-local correlation effects. To obtain the electronic DOS, we take the local part of the lattice Green's function $G_v^{\text{loc}} = \frac{1}{N} \sum_{\mathbf{k}} G_{\mathbf{kv}}$ and perform an analytical continuation from Matsubara frequency space (v) to real energies (E) using the stochastic optimization method⁷⁴.

In the single-shot D-TRILEX calculations for the susceptibility the diagrammatic part of the polarization operator $\bar{\Pi}_{\mathbf{q}\omega}^{\zeta}$ is obtained non-self-consistently. In this case, $\bar{\Pi}_{\mathbf{q}\omega}^{\zeta}$ accounts only for DMFT Green's functions $G_{\mathbf{kv}}^D$ that are dressed by the local self-energies: $G_{\mathbf{kv}}^{D-1} = iv + \mu - \epsilon_{\mathbf{k}} - \Sigma_v^{\text{imp}}$. Charge and spin susceptibilities $X_{\mathbf{q}\omega}^\zeta$ can then be obtained straightforwardly as $X_{\mathbf{q}\omega}^{\zeta-1} = \Pi_{\mathbf{q}\omega}^{\zeta-1} - U_{\mathbf{q}\omega}^{\zeta}$ ⁴⁵. We note that this form of the D-TRILEX susceptibility resembles the DMFT susceptibility^{75–77} with a longitudinal dynamical vertex corrections⁴⁴.

DATA AVAILABILITY

The data that support the findings of this work are available from the corresponding author upon reasonable request.

CODE AVAILABILITY

First-principle calculations have been performed on the basis of VASP^{59,60} and QUANTUM ESPRESSO⁶⁹ codes that can be requested from the developers. Many-body calculations have been performed using the implementation of the D-TRILEX method^{43,44} that can be obtained from the corresponding authors upon reasonable request.

Received: 18 January 2022; Accepted: 21 April 2022;

Published online: 24 May 2022

REFERENCES

1. Bandurin, D. A. et al. High electron mobility, quantum Hall effect and anomalous optical response in atomically thin InSe. *Nat. Nanotechnol.* **12**, 223–227 (2017).
2. Sucharitakul, S. et al. Intrinsic electron mobility exceeding $10^3 \text{ cm}^2/(\text{V s})$ in multilayer InSe FETs. *Nano Lett.* **15**, 3815–3819 (2015).
3. Tamalampudi, S. R. et al. High performance and bendable few-layered InSe photodetectors with broad spectral response. *Nano Lett.* **14**, 2800–2806 (2014).

4. Mudd, G. W. et al. The direct-to-indirect band gap crossover in two-dimensional van der Waals Indium Selenide crystals. *Sci. Rep.* **6**, 39619 (2016).
5. Hung, N. T., Nugraha, A. R. T. & Saito, R. Two-dimensional InSe as a potential thermoelectric material. *Appl. Phys. Lett.* **111**, 092107 (2017).
6. Shang, J. et al. Tunable electronic and optical properties of InSe/InTe van der Waals heterostructures toward optoelectronic applications. *J. Mater. Chem. C* **6**, 7201–7206 (2018).
7. Zólyomi, V., Drummond, N. D. & Fal'ko, V. I. Electrons and phonons in single layers of hexagonal indium chalcogenides from ab initio calculations. *Phys. Rev. B* **89**, 205416 (2014).
8. Kibirev, I. A., Matetskiy, A. V., Zotov, A. V. & Saranin, A. A. Thickness-dependent transition of the valence band shape from parabolic to Mexican-hat-like in the MBE grown InSe ultrathin films. *Appl. Phys. Lett.* **112**, 191602 (2018).
9. Henck, H. et al. Evidence of direct electronic band gap in two-dimensional van der Waals indium selenide crystals. *Phys. Rev. Mater.* **3**, 034004 (2019).
10. Irkhin, V. Y., Katanin, A. A. & Katsnelson, M. I. Effects of van Hove singularities on magnetism and superconductivity in the $t - t'$ Hubbard model: A parquet approach. *Phys. Rev. B* **64**, 165107 (2001).
11. Kampf, A. P. & Katanin, A. A. Competing phases in the extended $U - V - J$ Hubbard model near the Van Hove fillings. *Phys. Rev. B* **67**, 125104 (2003).
12. Metzner, W., Salmhofer, M., Honerkamp, C., Meden, V. & Schönhammer, K. Functional renormalization group approach to correlated fermion systems. *Rev. Mod. Phys.* **84**, 299–352 (2012).
13. Cao, Y. et al. Unconventional superconductivity in magic-angle graphene superlattices. *Nature* **556**, 43–50 (2018).
14. Cao, Y. et al. Correlated insulator behaviour at half-filling in magic-angle graphene superlattices. *Nature* **556**, 80–84 (2018).
15. Yankowitz, M. et al. Tuning superconductivity in twisted bilayer graphene. *Science* **363**, 1059–1064 (2019).
16. Yudin, D. et al. Fermi condensation near van Hove singularities within the Hubbard model on the triangular lattice. *Phys. Rev. Lett.* **112**, 070403 (2014).
17. Lugovskoi, A. V., Katsnelson, M. I. & Rudenko, A. N. Strong electron-phonon coupling and its influence on the transport and optical properties of hole-doped single-layer InSe. *Phys. Rev. Lett.* **123**, 176401 (2019).
18. Alidoosti, M., Esfahani, D. N. & Asgari, R. Charge density wave and superconducting phase in monolayer InSe. *Phys. Rev. B* **103**, 035411 (2021).
19. Iordanidou, K. et al. Hole-doped 2D InSe for spintronic applications. *ACS Appl. Nano Mater.* **1**, 6656–6665 (2018).
20. Ceferino, A. et al. Tunable spin-orbit coupling in two-dimensional InSe. *Phys. Rev. B* **104**, 125432 (2021).
21. Zólyomi, V., Drummond, N. D. & Fal'ko, V. I. Electrons and phonons in single layers of hexagonal indium chalcogenides from ab initio calculations. *Phys. Rev. B* **89**, 205416 (2014).
22. Li, G., Antipov, A. E., Rubtsov, A. N., Kirchner, S. & Hanke, W. Competing phases of the Hubbard model on a triangular lattice: Insights from the entropy. *Phys. Rev. B* **89**, 161118 (2014).
23. Das Sarma, S. & Hwang, E. H. Screening and transport in 2D semiconductor systems at low temperatures. *Sci. Rep.* **5**, 16655 (2015).
24. Katsnelson, M. I. *The Physics of Graphene* 2nd edn (Cambridge University Press, 2020).
25. Andersen, K., Latini, S. & Thygesen, K. S. Dielectric Genome of van der Waals Heterostructures. *Nano Lett.* **15**, 4616–4621 (2015).
26. Rösner, M., Şəsioglu, E., Friedrich, C., Blügel, S. & Wehling, T. O. Wannier function approach to realistic Coulomb interactions in layered materials and heterostructures. *Phys. Rev. B* **92**, 085102 (2015).
27. Wehling, T. O. et al. Strength of Effective Coulomb Interactions in Graphene and Graphite. *Phys. Rev. Lett.* **106**, 236805 (2011).
28. van Loon, E. G. C. P., Rösner, M., Schönhoff, G., Katsnelson, M. I. & Wehling, T. O. Competing Coulomb and electron-phonon interactions in NbS₂. *npj Quantum Mater.* **3**, 1–8 (2018).
29. Vonsovsky, S. V. & Katsnelson, M. I. Some types of instabilities in the electron energy spectrum of the polar model of the crystal. I. The maximum-polarity state. *J. Phys. C: Solid State Phys.* **12**, 2043–2053 (1979).
30. Zhang, Y. & Callaway, J. Extended Hubbard model in two dimensions. *Phys. Rev. B* **39**, 9397–9404 (1989).
31. Nomura, Y. & Arita, R. Ab initio downfolding for electron-phonon-coupled systems: Constrained density-functional perturbation theory. *Phys. Rev. B* **92**, 245108 (2015).
32. Berger, E., Valášek, P. & von der Linden, W. Two-dimensional Hubbard-Holstein model. *Phys. Rev. B* **52**, 4806–4814 (1995).
33. Sangiovanni, G., Capone, M., Castellani, C. & Grilli, M. Electron-phonon interaction close to a mott transition. *Phys. Rev. Lett.* **94**, 026401 (2005).
34. Werner, P. & Millis, A. J. Efficient dynamical mean field simulation of the Holstein-Hubbard model. *Phys. Rev. Lett.* **99**, 146404 (2007).
35. Pines, D. & Nozieres, P. *The theory of quantum liquids: normal fermi liquids. theory of quantum liquids* (W.A. Benjamin, Philadelphia, 1966).
36. Platzman, P. M. & Wolff, P. A. Waves and interactions in solid state plasmas, vol. 13 (Academic Press, New York, 1973).
37. Vonsovsky, S. V. & Katsnelson, M. I. Quantum solid-state physics (Springer Verlag, Berlin, 1989).
38. Hedin, L. New method for calculating the one-particle green's function with application to the electron-gas problem. *Phys. Rev.* **139**, A796–A823 (1965).
39. Aryasetiawan, F. & Gunnarsson, O. The GW method. *Rep. Prog. Phys.* **61**, 237 (1998).
40. Hedin, L. On correlation effects in electron spectroscopies and the GW approximation. *J. Phys. Condens. Matter* **11**, R489 (1999).
41. Georges, A., Kotliar, G., Krauth, W. & Rozenberg, M. J. Dynamical mean-field theory of strongly correlated fermion systems and the limit of infinite dimensions. *Rev. Mod. Phys.* **68**, 13–125 (1996).
42. Rohringer, G. et al. Diagrammatic routes to nonlocal correlations beyond dynamical mean field theory. *Rev. Mod. Phys.* **90**, 025003 (2018).
43. Stepanov, E. A., Harkov, V. & Lichtenstein, A. I. Consistent partial bosonization of the extended Hubbard model. *Phys. Rev. B* **100**, 205115 (2019).
44. Harkov, V., Vandelli, M., Brener, S., Lichtenstein, A. I. & Stepanov, E. A. Impact of partially bosonized collective fluctuations on electronic degrees of freedom. *Phys. Rev. B* **103**, 245123 (2021).
45. Vandelli, M. et al. Multi-band D-TRILEX approach to materials with strong electronic correlations. <https://arxiv.org/abs/2204.06426> (2022).
46. Stepanov, E. A., Nomura, Y., Lichtenstein, A. I. & Biermann, S. Orbital isotropy of magnetic fluctuations in correlated electron materials induced by Hund's exchange coupling. *Phys. Rev. Lett.* **127**, 207205 (2021).
47. Efetov, D. K. & Kim, P. Controlling electron-phonon interactions in graphene at ultrahigh carrier densities. *Phys. Rev. Lett.* **105**, 256805 (2010).
48. Crowther, A. C., Ghassaei, A., Jung, N. & Brus, L. E. Strong charge-transfer doping of 1 to 10 layer graphene by NO₂. *ACS Nano* **6**, 1865–1875 (2012).
49. Vandelli, M. et al. Extended regime of coexisting metallic and insulating phases in a two-orbital electronic system. <https://arxiv.org/abs/2204.02116> (2022).
50. Stepanov, E. A. Eliminating orbital selectivity from the metal-insulator transition by strong magnetic fluctuations. <https://arxiv.org/abs/2204.02895> (2022).
51. Keldysh, L. V. & Kopaev, Y. V. Possible instability of semimetallic state toward Coulomb interaction. *Soviet Phys. Solid State* **6**, 2219 (1965).
52. Kozlov, A. N. & Maksimov, L. A. The metal-dielectric divalent crystal phase transition. *Sov. Phys. JETP* **21**, 790 (1965).
53. Halperin, B. I. & Rice, T. M. The excitonic state at the semiconductor-semimetal transition. In *Solid State Physics*, vol. 21, 115–192 (Academic Press, 1968). <https://www.sciencedirect.com/science/article/pii/S0081194708607407>.
54. Irkhin, V. Y. & Katsnelson, M. I. Current carriers in a quantum two-dimensional antiferromagnet. *J. Phys. Condens. Matter* **3**, 6439–6453 (1991).
55. Rudenko, A. N., Stepanov, E. A., Lichtenstein, A. I. & Katsnelson, M. I. Excitonic instability and pseudogap formation in nodal line semimetal ZrSiS. *Phys. Rev. Lett.* **120**, 216401 (2018).
56. Waldecker, L. et al. Rigid band shifts in two-dimensional semiconductors through external dielectric screening. *Phys. Rev. Lett.* **123**, 206403 (2019).
57. Blöchl, P. E. Projector augmented-wave method. *Phys. Rev. B* **50**, 17953–17979 (1994).
58. Kresse, G. & Joubert, D. From ultrasoft pseudopotentials to the projector augmented-wave method. *Phys. Rev. B* **59**, 1758–1775 (1999).
59. Kresse, G. & Furthmüller, J. Efficiency of ab-initio total energy calculations for metals and semiconductors using a plane-wave basis set. *Comput. Mater. Sci.* **6**, 15–50 (1996).
60. Kresse, G. & Furthmüller, J. Efficient iterative schemes for ab initio total-energy calculations using a plane-wave basis set. *Phys. Rev. B* **54**, 11169–11186 (1996).
61. Perdew, J. P., Burke, K. & Ernzerhof, M. Generalized gradient approximation made simple. *Phys. Rev. Lett.* **77**, 3865–3868 (1996).
62. Marzari, N. & Vanderbilt, D. Maximally localized generalized Wannier functions for composite energy bands. *Phys. Rev. B* **56**, 12847–12865 (1997).
63. Marzari, N., Mostofi, A. A., Yates, J. R., Souza, I. & Vanderbilt, D. Maximally localized Wannier functions: Theory and applications. *Rev. Mod. Phys.* **84**, 1419–1475 (2012).
64. Mostofi, A. A. et al. wannier90: a tool for obtaining maximally localised Wannier functions. *Comput. Phys. Commun.* **178**, 685–699 (2008).
65. Miyake, T. & Aryasetiawan, F. Screened coulomb interaction in the maximally localized wannier basis. *Phys. Rev. B* **77**, 085122 (2008).
66. Kaltak, M. Merging GW with DMFT (2015). <http://theses.univie.ac.at/38099/>. PhD Thesis, University of Vienna, 2015, 231 pp.
67. Resta, R. Thomas-Fermi dielectric screening in semiconductors. *Phys. Rev. B* **16**, 2717–2722 (1977).
68. Keldysh, L. V. Coulomb interaction in thin semiconductor and semimetal films. *JETP Lett.* **29**, 658 (1979). [*Pis'ma Zh. Eksp. Teor. Fiz.* **29**, 716 (1979)].

69. Giannozzi, P. et al. Advanced capabilities for materials modelling with Quantum ESPRESSO. *J. Phys. Condens. Matter* **29**, 465901 (2017).
70. Poncé, S., Margine, E. R., Verdi, C. & Giustino, F. EPW: electron-phonon coupling, transport and superconducting properties using maximally localized Wannier functions. *Comput. Phys. Commun.* **209**, 116–133 (2016).
71. Hafermann, H., Werner, P. & Gull, E. Efficient implementation of the continuous-time hybridization expansion quantum impurity solver. *Comput. Phys. Commun.* **184**, 1280–1286 (2013).
72. Hafermann, H. Self-energy and vertex functions from hybridization-expansion continuous-time quantum monte carlo for impurity models with retarded interaction. *Phys. Rev. B* **89**, 235128 (2014).
73. Bauer, B. et al. The ALPS project release 2.0: open source software for strongly correlated systems. *J. Stat. Mech.: Theory Exp.* **2011**, P05001 (2011).
74. Krivenko, I. & Harland, M. TRIQS/SOM: implementation of the stochastic optimization method for analytic continuation. *Comput. Phys. Commun.* **239**, 166–183 (2019).
75. Boehnke, L. & Lechermann, F. Competing orders in Na_xCoO_2 from strong correlations on a two-particle level. *Phys. Rev. B* **85**, 115128 (2012).
76. Boehnke, L., Werner, P. & Lechermann, F. Multi-orbital nature of the spin fluctuations in Sr_2RuO_4 . *Europhys. Lett.* **122**, 57001 (2018).
77. Strand, H. U. R., Zingl, M., Wentzell, N., Parcollet, O. & Georges, A. Magnetic response of Sr_2RuO_4 : Quasi-local spin fluctuations due to Hund's coupling. *Phys. Rev. B* **100**, 125120 (2019).

ACKNOWLEDGEMENTS

We thank Andy J. Millis for fruitful discussions, Jan Berges for sharing his cDFPT-related changes to QUANTUM ESPRESSO with us, and Igor Krivenko for technical support of SOM. The work of E.A.S. was supported by the European Union's Horizon 2020 Research and Innovation programme under the Marie Skłodowska Curie grant agreement No. 839551 - 2DMAGICS. The work of M.I.K., A.N.R., and A.I.L. was supported by European Research Council via Synergy Grant 854843 - FASTCORR. V.H. and A.I.L. acknowledge the support by the Cluster of Excellence "Advanced Imaging of Matter" of the Deutsche Forschungsgemeinschaft (DFG) - EXC 2056 - Project No. ID390715994. E.A.S., V.H., and A.I.L. also acknowledge the support by North-German Supercomputing Alliance (HLRN) under the Project No. hhp00042.

AUTHOR CONTRIBUTIONS

All authors discussed the results and contributed to the preparation of the manuscript.

COMPETING INTERESTS

The authors declare no competing interests.

ADDITIONAL INFORMATION

Correspondence and requests for materials should be addressed to Evgeny A. Stepanov or Alexander N. Rudenko.

Reprints and permission information is available at <http://www.nature.com/reprints>

Publisher's note Springer Nature remains neutral with regard to jurisdictional claims in published maps and institutional affiliations.



Open Access This article is licensed under a Creative Commons Attribution 4.0 International License, which permits use, sharing, adaptation, distribution and reproduction in any medium or format, as long as you give appropriate credit to the original author(s) and the source, provide a link to the Creative Commons license, and indicate if changes were made. The images or other third party material in this article are included in the article's Creative Commons license, unless indicated otherwise in a credit line to the material. If material is not included in the article's Creative Commons license and your intended use is not permitted by statutory regulation or exceeds the permitted use, you will need to obtain permission directly from the copyright holder. To view a copy of this license, visit <http://creativecommons.org/licenses/by/4.0/>.

© The Author(s) 2022